energies

MDPI

Article

Effect of Geometric Configurations of Molten-Salt Risers on Its Hydraulic and Structural Behavior in Tower-Based Concentrated Solar Power Station

Yida Liu [1,2], Zijiang Yang [3], Jinsheng Qi [1], Xiaoliang Li [1], Junxiang Xu [1] and Zhan Wang [3,*]

[1] Shandong Electric Power Engineering Consulting Institute Co., Ltd., Jinan 250013, China; liuyida@spic.com.cn (Y.L.); qijinsheng@spic.com.cn (J.Q.); lixiaoliang@spic.com.cn (X.L.); xujunxiang01@spic.com.cn (J.X.)
[2] State Key Laboratory of Engines, Tianjin University, Tianjin 300072, China
[3] School of Nuclear Science, Energy and Power Engineering, Shandong University, Jinan 250061, China; 202534634@mail.sdu.edu.cn
* Correspondence: wangzhan@sdu.edu.cn

Abstract

Geometric configuration influences the hydraulic performance, structural response, and material requirements of molten-salt risers in tower-based concentrated solar power plants. However, the effects of the principal geometric parameters on the hydraulic and structural responses of a complete riser system have not been sufficiently clarified. In this study, a full-scale molten-salt riser model was established under fixed total-height and lateral-space constraints. Thirteen configurations were generated using a single-factor parametric design, and computational fluid dynamics and structural finite-element simulations were employed to investigate the effects of the inclined-segment length-to-diameter ratio L_s/D_i, elbow curvature ratio R/D_i, and inclined-segment angle θ. The results show that increasing L_s/D_i increases the overall system resistance coefficient but reduces the maximum von Mises equivalent stress under the combined load case by up to 17.12%. Increasing R/D_i reduces both the overall system resistance coefficient and the combined-load maximum stress, while the maximum total deformation and pipe mass change only slightly. Increasing θ increases the overall system resistance coefficient but decreases the combined-load maximum total deformation, whereas the combined-load maximum stress varies nonmonotonically and reaches a minimum of 194.95 MPa at $\theta = 75°$. These results clarify the distinct hydraulic and structural response trends associated with the three geometric parameters. Among the investigated configurations, the 45° configuration demonstrates a degree of coordination among hydraulic performance, structural response, and pipe material usage. The findings provide a numerical basis for the configuration design and parameter selection of molten-salt risers in tower-based concentrated solar power plants.

Keywords: tower-based concentrated solar power plant; molten-salt riser; inclined pipe segment; inclined-segment angle; flow resistance; structural response

Check for updates

Academic Editor: Maria Vicidomini

Received: 27 September 2026
Revised: 21 October 2026
Accepted: 28 October 2026
Published: 30 October 2026

Copyright: © 2026 by the authors. Licensee MDPI, Basel, Switzerland. This article is an open access article distributed under the terms and conditions of the Creative Commons Attribution (CC BY) license.

1. Introduction

The global energy system is undergoing a structural transformation centered on the development of clean and low-carbon energy sources. The large-scale development and utilization of renewable energy have become important approaches to addressing climate change and ensuring energy security. As one of the renewable energy sources with considerable resource potential and wide geographic distribution, solar energy provides im-

portant support for the low-carbon transition of the energy structure through its efficient large-scale utilization. Concentrated solar power (CSP) technology can be classified into parabolic-trough, tower-based, linear-Fresnel, and parabolic-dish [1]. The majority of newly commissioned power plants in China have adopted the tower-based CSP technology, which offers superior thermal efficiency. In tower-based CSP plants, a heliostat field focuses incident solar radiation onto a centrally located receiver mounted atop the tower, thereby heating molten salt to high temperatures. The thermally charged molten salt is subsequently stored in a high-temperature thermal energy storage (TES) system and later discharged to generate steam via a heat exchanger, driving a conventional Rankine-cycle turbine generator. This configuration constitutes one of the principal technological pathways for large-scale, dispatchable thermal energy storage in CSP systems. At the system level, continuity of high-temperature thermal delivery depends on the coordinated operation of solar-energy collection, thermal transport, and TES charging and discharging. For example, Cristaudo et al. showed that the coordinated charging and discharging of a dual-rock-bed TES system can support continuity between solar-energy collection and thermal-load delivery [2], illustrating the role of storage management and the associated transport loop in the operation of integrated solar thermal systems. Within the molten-salt circulation loop, cold-phase molten salt is pumped upward through the riser pipe to the tower-mounted receiver, where it absorbs concentrated solar energy; the heated (hot-phase) salt then flows downward via the downcomer pipe to the ground-level thermal energy storage tanks [3]. As a critical transport conduit linking the ground-level system to the tower-top receiver, the molten-salt riser is characterized by substantial elevation gain, high operating temperatures, and spatially constrained piping layout. Constrained by tower height and lateral spatial limitations, the riser typically comprises vertical segments, inclined pipe segments, and multiple elbows. Consequently, its geometric configuration governs both flow resistance and high-temperature structural behavior of the piping system. Flow-direction changes at elbows introduce additional local pressure losses, the magnitudes of which depend sensitively on geometric parameters—including bend angle and curvature radius. Furthermore, the discontinuity in curvature at elbow transitions induces elevated local stresses under the combined actions of internal pressure, gravitational loading, and thermal expansion. As a result, any given geometric parameter concurrently influences both hydraulic performance and structural integrity of the riser; thus, evaluating the configuration using a single performance metric fails to comprehensively capture its operational behavior.

Extensive research has established a robust foundation for understanding the relationship between elbow geometric parameters and flow-induced pressure losses in systems using conventional working fluids. Itō [4] and Idelchik [5] pioneered the experimental characterization and systematic compilation of local pressure loss correlations and engineering calculation methods for pipe elbows. More recently, Zhang et al. [6] investigated pressure loss and secondary flow development in curved pipes using ambient-temperature air as the working fluid; they reported that the global pressure drop exhibited a nonmonotonic trend—first increasing, then decreasing, and finally increasing again—with increasing bend angle. Among six representative bend angles ranging from 0° to 180°, the 90° configuration produced the most pronounced secondary flow. In parallel, Du et al. [7] examined how bend angle affects swirl structure and found that, within the 0–90° range, larger bend angles intensify the Dean vortices downstream of the bend, resulting in greater vortex strength. Helmizar et al. [8] further demonstrated that the resistance coefficient of 90° elbows exhibits a pronounced nonlinear dependence on the curvature ratio using incompressible water as the working fluid. Analogous geometric effects—namely, curvature-ratio-driven nonlinearity in local pressure loss—have also been documented in superheated steam, supercritical water, and subcritical pressure aviation fuels [9–11]. However, existing thermal-hydraulic

studies of molten salts have predominantly addressed flow in straight pipes. Liu et al. [12] conducted experiments on turbulent flow of molten salt in a circular pipe, whereas Srivastava et al. [13] and Ferng et al. [14] separately validated the applicability of conventional friction correlations to FLiNaK flow in straight pipes. In contrast, studies on the local resistance, overall system resistance, and downstream flow fields of molten-salt elbows and risers with multiple elbows remain limited. The applicability of elbow-flow correlations developed for conventional working fluids to high-temperature molten-salt systems has not yet been directly validated.

In addition to affecting the internal flow characteristics, geometric configurations can also influence the load-carrying path and deformation characteristics of the riser, thereby rendering elbows critical regions in the structural response of high-temperature piping systems. Based on a parametric finite-element model, Li et al. [15] demonstrated that the bend angle affects the limit load-carrying capacity of elbows under different loading conditions. Wang et al. [16] further revealed that nonuniform wall thickness and cross-sectional ovality can cause the high-stress regions of elbows to shift. Kim et al. [17] subsequently confirmed the significant effects of geometric imperfections and wall-thickness variations on the failure behavior of elbows. In high-temperature piping systems, thermal loads and boundary constraints can further modify the distributions of stress and deformation. Existing studies indicate that local thermal stress and thermal deformation are influenced by the coupled effects of temperature variations, pipeline system constraints, and spatial positioning [18–20]. Meanwhile, the structural flexibility of pipeline systems and their response characteristics under combined loads (such as thermal and mechanical loads) have become critical factors that must be fully considered in structural assessments [21,22].

Beyond thermal-expansion and self-weight loads, the nonuniform wall pressure induced by internal flow also constitutes a direct mechanical load acting on the pipe wall. Under the combined effects of curvature and centrifugal forces, a spatially nonuniform wall-pressure distribution develops within the elbow. If a uniform internal pressure is used in the structural analysis, the differences in local fluid loads induced by different geometric configurations cannot be retained. Abuhatira et al. [23] developed a one-way fluid–structure interaction model coupling computational fluid dynamics and finite-element analysis (CFD–FEA) for a 90° elbow and transferred the flow-induced loads obtained from the CFD analysis to the structural model for response analysis. Solomon and Dundulis [24] likewise employed a one-way fluid–structure interaction method, using the pipe-wall pressure obtained from the CFD analysis as the input to the structural model. Collectively, these studies indicate that one-way fluid–structure interaction based on the transfer of the wall-pressure field can preserve the spatial distribution characteristics of fluid loads in structural analyses, thereby providing a feasible approach for comparing the structural responses of different elbow configurations.

Overall, the hydraulic characteristics of elbows with conventional working fluids and the structural responses of high-temperature piping systems have been extensively investigated. However, a systematic understanding of molten-salt risers in solar power tower plants remains limited. To date, existing studies on molten salt have primarily focused on straight pipes, whereas practical risers consist of continuous vertical segments, inclined pipe segments, and multiple elbows. Therefore, the flow characteristics derived from isolated elbow models cannot reliably represent the total pressure drop or accurately predict the downstream flow field of the full-scale riser assembly. Meanwhile, previous structural studies have mainly considered individual elbows or specific high-temperature piping systems, and a unified comparison of the variations in resistance, stress, and deformation induced by geometric parameters under a full-scale model is still lacking. Although one-way fluid–structure interaction methods based on the transfer of CFD pressure fields have been

applied to other piping problems, their application to the geometric-configuration analysis of molten-salt risers in tower-based solar thermal power plants remains limited.

In this study, a full-scale molten-salt riser pipe model was established under fixed total height and lateral spatial constraints. The elbow curvature ratio R/D_i, inclined-segment angle θ, and inclined-segment length-to-diameter ratio L_s/D_i were selected as the geometric variables, and 13 piping configurations were constructed using the one-factor-at-a-time method. First, the overall system resistance coefficient, downstream velocity and turbulent kinetic energy distributions, and pipe-wall pressure field were obtained through CFD simulations. The wall-pressure field was then transferred unidirectionally to the structural finite-element model. Subsequently, the non-thermal load case, thermal-expansion load case, and combined load case were established separately to obtain the maximum von Mises equivalent stress, maximum total deformation, and pipe mass for each configuration. By comparing the parameter–response curves alongside representative flow-field, stress-field, and deformation-field distributions, the response relationships among flow resistance, stress, deformation, and metal pipe mass corresponding to the three geometric parameters were analyzed. The results provide a numerical basis for the configuration design and parameter selection of molten-salt risers.

2. Model and Method

2.1. Physical Model

The physical model of the molten-salt riser established in this study is illustrated in Figure 1. The total height of the riser system is denoted by H_{total}. To minimize boundary effects on the flow characteristics within the region of interest, both the inlet and outlet straight pipe segments are configured with a length of 10D. The inclined-segment angle θ is defined as the angle between the centerline of the inclined pipe segment and the vertical direction, where $0 < \theta \leq 90°$. The radius of curvature along the elbow centerline is denoted by R, and the length of the inclined pipe segment centerline is denoted by L_s. The dimensionless parameters R/D_i and L_s/D_i are employed to characterize the elbow curvature radius and equivalent inclined-segment length, respectively. When R/D_i, θ, or L_s/D_i is varied, the lengths of the adjacent vertical pipe segments are adjusted to maintain a constant total vertical extent. Namely, the sum of vertical projections of the centerlines of all pipe segments remains equal to H_{total}, thereby ensuring a consistent total height among the different configurations we studied. Additionally, to comply with the internal spatial layout constraints of the receiver tower, the riser system is subject to a prescribed lateral-space boundary.

2.2. Single-Factor Parametric Design

To compare the single-factor response trends under the prescribed geometric closure constraints of elbow curvature radius (R/D_i), inclined-segment angle (θ), and equivalent inclined-segment length (L_s/D_i) on the hydraulic performance, structural response, and pipe material usage of the molten-salt riser system, a one-factor-at-a-time parametric design method was conducted. The elbow curvature ratio $R/D_i = 3.25$, inclined-segment angle $\theta = 45°$, and inclined-section length-to-diameter ratio $L_s/D_i = 14.706$ were selected as the baseline configuration.

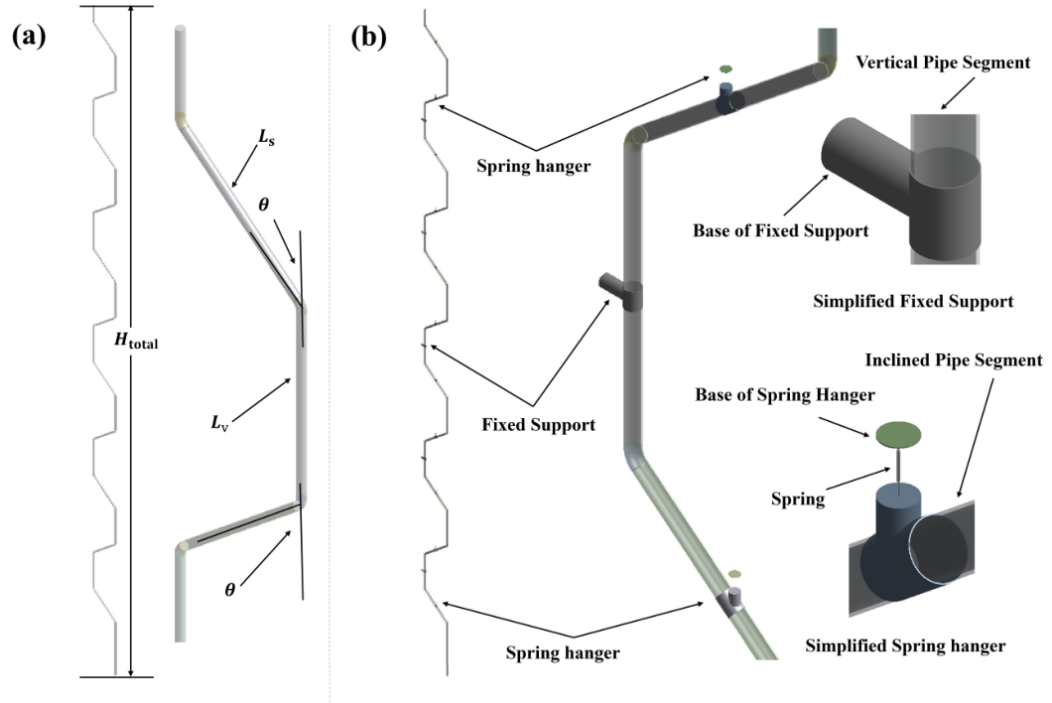


Figure 1. Schematic of the geometric configuration and computational domains of the molten-salt riser: (**a**) CFD fluid computational domain including the inlet and outlet segments; (**b**) structural finite-element computational domain and local structural connection configuration.

In the parametric analysis, only one geometric parameter was varied at a time while the other two were held constant at their baseline values. The elbow curvature ratio R/D_i was varied across 1.50, 2.00, 2.50, 3.00, and 3.25; the inclined-segment angle θ across 30°, 45°, 60°, 75°, and 90°; and the inclined-segment length-to-inner-diameter ratio L_s/D_i across 10.695, 14.706, 18.717, 22.727, and 26.471. Each parameter was assigned five discrete levels, with the baseline configuration common to all three parameter sets. Excluding the duplicated baseline case, a total of 13 distinct riser configurations were generated. The corresponding parameter values are presented in Table 1.

Table 1. Single-factor parametric design of molten-salt riser and geometric parameters for each configuration.

ID	θ/°	R/D_i	L_s/D_i	Remarks
0	45	3.25	14.706	Baseline configuration
1	45	1.5	14.706	
2	45	2	14.706	
3	45	2.5	14.706	
4	45	3	14.706	
5	30	3.25	14.706	
6	60	3.25	14.706	
7	75	3.25	14.706	
8	90	3.25	14.706	
9	45	3.25	10.695	
10	45	3.25	18.717	
11	45	3.25	22.727	
12	45	3.25	26.471	

Note: D_i = 374 mm and D_o = 426 mm.

For each configuration, the total riser height H_{total} was fixed at 165 m, and the maximum horizontal footprint was constrained to 8 m. For analytical clarity, the molten-salt mass flow rate, the pipe inner diameter and the pipe wall thickness were held constant across all 13 riser-pipe configurations listed in Table 1. When R/D_i, θ, or L_s/D was varied, the dimensions of the associated pipe segments were adjusted in accordance with the geometric closure condition of the pipe centerlines, ensuring that all configurations concurrently satisfy both the total-height constraint (H_{total} = 165 m) and the lateral-space constraint (maximum footprint ≤ 8 m). Consequently, hydraulic and structural response differences arising from geometric parameter variations can be meaningfully compared under consistent global layout conditions.

Figure 2 presents superimposed geometric configurations of a representative return-bend unit to illustrate the geometric variations listed in Table 1.

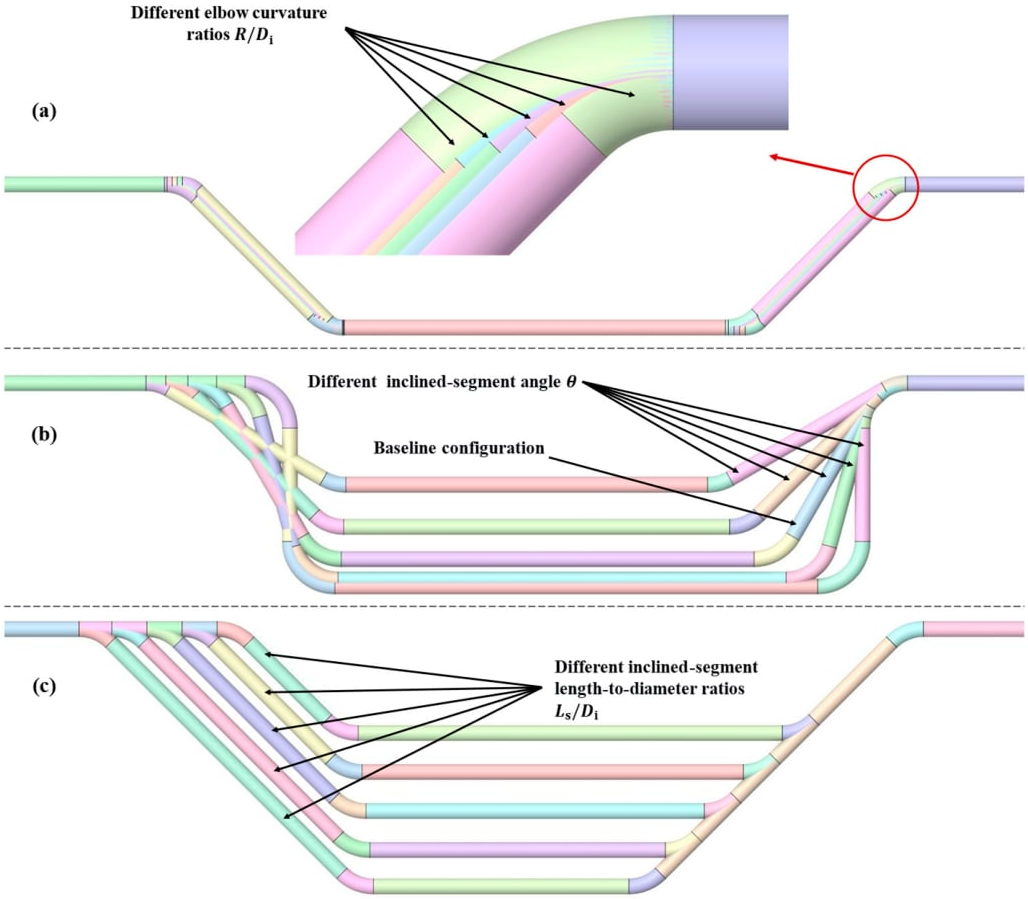


Figure 2. Superimposed geometric configurations of a representative return-bend unit: (**a**) different elbow curvature ratios R/D_i; (**b**) different inclined-segment angles θ; (**c**) different inclined-segment length-to-diameter ratios L_s/D_i.

2.3. Numerical Calculation Models and Boundary Conditions

2.3.1. CFD Model and Hydraulic Indicators

Steady-state numerical simulations of the flow inside the molten-salt riser were performed using ANSYS Fluent 15.0 (ANSYS, Inc., Canonsburg, PA, USA). The working fluid was a binary nitrate salt consisting of 60 wt.% $NaNO_3$ and 40 wt.% KNO_3. The design operating temperature of the riser in the reference plant was 295 °C. Because the present study focuses on the hydraulic behavior under the normal design condition and neglects the heat loss from the insulated riser, an isothermal flow model was adopted and the energy equation was not solved. The density and dynamic viscosity were assigned constant values

evaluated at 295 °C, namely, 1902.5 kg·m^{-3} and 0.00338 Pa·s, respectively. The molten salt was modeled as an incompressible Newtonian fluid, with its properties held uniform and constant throughout the computational domain. The fluid flow was described by the continuity and momentum equations.

$$\nabla \cdot (\rho \, \boldsymbol{u}) = 0$$

$$\rho(\boldsymbol{u}\cdot\nabla)\boldsymbol{u} = -\nabla p + \mu\nabla^2\boldsymbol{u} + \rho\mathbf{g}$$

where $\boldsymbol{u}$ is the velocity vector, p is the pressure, μ is the dynamic viscosity of the fluid, and $\mathbf{g}$ is the gravitational acceleration vector.

The momentum equation was solved using the Reynolds-averaged Navier–Stokes (RANS) formulation. Turbulence closure was achieved with the realizable k–ε model, and a non-equilibrium wall function was applied to resolve the near-wall flow behavior [25].

The flow boundary conditions were specified according to the engineering design data of the reference tower-based CSP plant. A mass-flow inlet of 798.889 kg·s^{-1} was imposed, corresponding to the design molten-salt flow rate of the riser under the normal operating condition. A pressure outlet of 3.7 MPa was specified. This value was obtained by converting the plant design pressure to the outlet location of the modeled riser section according to the design pressure distribution of the molten-salt loop. The pipe wall was assigned a no-slip boundary condition. The equivalent sand-grain roughness height and roughness constant were set to 0.07 mm and 0.5, respectively. The gravitational acceleration was set to 9.807 m·s^{-2} in the vertically downward direction. A pressure-based steady-state solver was employed. Pressure–velocity coupling was achieved using the Coupled scheme, and the gradient terms were discretized using the cell-based least-squares method. The pressure, momentum, turbulent kinetic energy, and turbulent dissipation rate equations were discretized using second-order schemes. The residual convergence criterion was set to 10^{-6}.

The principal characteristics, boundary conditions, and numerical settings of the CFD model are summarized in Table 2.

Table 2. Principal characteristics, boundary conditions, and numerical settings of the CFD model.

Category	Item	Setting
Fluid model	Working fluid	60 wt.% $NaNO_3$–40 wt.% KNO_3
Fluid model	Flow assumption	Steady, isothermal, incompressible, and Newtonian
Fluid model	Design operating temperature	295 °C
Fluid model	Energy equation	Not solved
Fluid properties	Density at 295 °C	1902.5 kg·m^{-3}
Fluid properties	Dynamic viscosity at 295 °C	0.00338 Pa·s
Turbulence model	Turbulence closure	Realizable k-ε model
Turbulence model	Near-wall treatment	Non-equilibrium wall function
Boundary condition	Inlet	Mass-flow inlet, 798.889 kg·s^{-1}
Boundary condition	Outlet	Pressure outlet, 3.7 MPa
Boundary condition	Pipe wall	No-slip
Wall roughness	Equivalent sand-grain roughness height	0.07 mm
Wall roughness	Roughness constant	0.5
Body force	Gravitational acceleration	9.807 m·s^{-2}, vertically downward
Solver	Solver type	Pressure-based, steady-state
Solver	Pressure–velocity coupling	Coupled scheme
Spatial discretization	Gradient	Cell-based least-squares method
Spatial discretization	Pressure	Second-order
Spatial discretization	Momentum	Second-order upwind
Spatial discretization	Turbulent kinetic energy	Second-order upwind
Spatial discretization	Turbulent dissipation rate	Second-order upwind
Convergence	Residual criterion	10^{-6}

The overall system resistance coefficient K_{sys} was used to evaluate the hydraulic performance of different configurations and was defined as follows:

$$K_{sys} = \frac{\Delta p_{sys}}{0.5\rho v^2}$$

where Δp_{sys} is the pressure loss between the system inlet and outlet, and v is the cross-sectional average velocity.

2.3.2. Structural Finite-Element Model

A structural finite-element model of the molten-salt riser was established using ANSYS Mechanical. The pipe and elbows were both made of SA-106 Gr. B carbon steel, and an isotropic linear-elastic material model was employed. The material properties were determined in accordance with Section II, Part D of the ASME Boiler and Pressure Vessel Code [26] and are summarized in Table 3.

Table 3. Material properties used in the structural finite-element model.

Property	Symbol	Value	Unit
Material	—	SA-106 Gr. B carbon steel	—
Material model	—	Isotropic linear elastic	—
Density	ρ_s	7750	kg·m^{-3}
Elastic modulus at 295 °C	E	185.4	GPa
Poisson's ratio	ν	0.30	—
Coefficient of linear thermal expansion	α	1.33×10^{-5}	°C^{-1}

For the structural thermal analysis, the stress-free reference temperature was set to 22 °C, while a spatially uniform operating temperature of 295 °C was applied. The reference temperature defines the state at which the thermal strain is zero. For the constant coefficient of linear thermal expansion adopted in the present model, the thermal strain was expressed as

$$\varepsilon_{th} = \alpha(T - T_{ref})\mathbf{I}$$

where α is the coefficient of linear thermal expansion, T is the applied pipe temperature, T_{ref} is the stress-free reference temperature, and $\mathbf{I}$ is the identity tensor. The prescribed structural temperature difference was therefore 273 °C. The value of 22 °C was used only in the structural thermal-expansion calculation.

Simplified solid representations of the support-and-hanger assemblies were incorporated into the structural model to reflect the piping support configuration, as illustrated in Figure 1b. For the vertical pipe segments, the support arrangement consisted of a simplified fixed-support assembly and a solid clamp in contact with the outer pipe surface. The inner surface of the clamp was established in geometric contact with the corresponding outer surface of the pipe, and a frictional contact condition with a coefficient of friction of 0.30 was assigned to this interface. The fixed boundary condition was applied to the base face of the fixed-support assembly. At the clamp location, transverse pipe movement was constrained, whereas limited relative sliding along the local pipe-axis direction was permitted and resisted by friction. For the inclined pipe segment, an equivalent spring support with a stiffness of 275 N·mm^{-1} was assigned to represent the support flexibility, and the fixed boundary condition of the spring-hanger assembly was applied at its base. Fixed constraints were applied to both the inlet and outlet end faces of the pipe. The full pipe-wall pressure field obtained from the CFD simulations was mapped unidirectionally onto the inner surface of the structural pipe model, as shown in Figure 3. This transfer retained

the spatial pressure distribution associated with the prescribed outlet pressure, gravity, and flow through the riser. The uniform temperature load and support constraints were specified independently in the structural model, and structural self-weight was included by applying a vertically downward gravitational acceleration of 9.807 m·s^{-2}. Structural deformation was not transferred back to the CFD model.

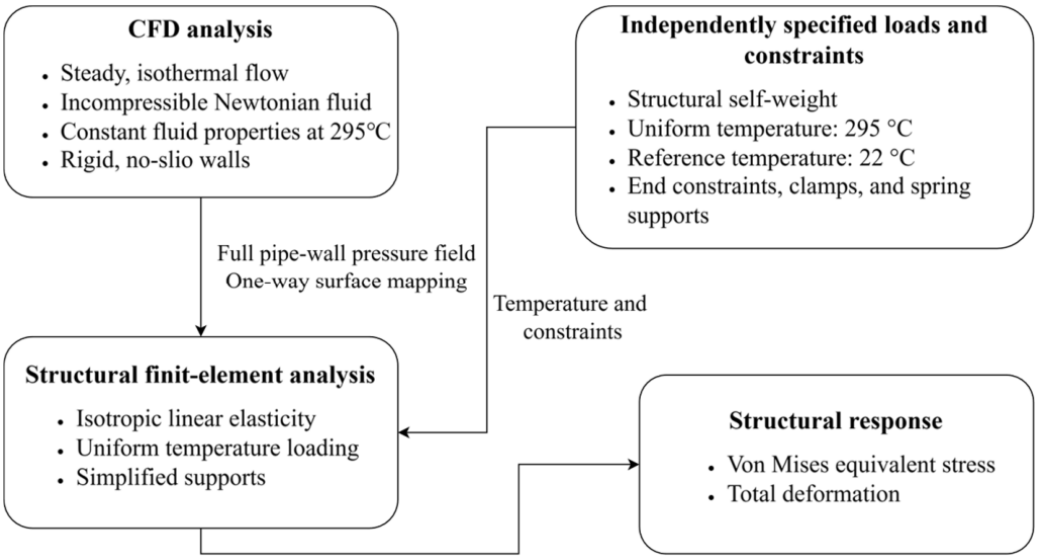


Figure 3. Schematic of the one-way pressure transfer between the CFD and structural finite-element models.

A limited sensitivity check was conducted using the baseline configuration to evaluate the effects of the friction coefficient and spring stiffness on the calculated structural response. The friction coefficient was varied from 0.24 to 0.36 while the spring stiffness was fixed at 275 N·mm^{-1}. The maximum total deformation ranged from 139.92 to 140.00 mm, and the maximum von Mises equivalent stress ranged from 208.75 to 208.85 MPa. The spring stiffness was then varied from 200 to 350 N·mm^{-1} while the friction coefficient was fixed at 0.30. The corresponding ranges were 139.93–140.10 mm for the maximum total deformation and 208.62–208.95 MPa for the maximum von Mises equivalent stress. Relative to the baseline results obtained with a friction coefficient of 0.30 and a spring stiffness of 275 N·mm^{-1}, the maximum relative deviations in the two structural indicators were below 0.1%.

Based on the aforementioned load combinations, three distinct analytical cases were defined: the non-thermal load case, the thermal-expansion load case, and the combined-load case. The non-thermal load case incorporates the structural self-weight and the CFD-derived wall-pressure field but excluding any thermal-expansion loading. The thermal-expansion load case represents the structural response to a uniform pipe temperature of 295 °C relative to the assumed stress-free reference temperature of 22 °C, with gravity and pressure loads excluded. The combined-load case superimposes the non-thermal loads defined previously with a uniform thermal-expansion loading. During post-processing, the stress-singularity-affected regions were excluded from the peak-stress comparison. These regions include the zones within $5D_i$ from the inlet and outlet end faces and the zones within $\pm 1D_i$ of each support/hanger attachment location. The von Mises equivalent stress and total deformation of the piping structure were then extracted for the three load cases. Furthermore, the masses of the pipe and elbow solids in each structural model were extracted to compare the relative steel material usage among the different configurations.

The present CFD–FEA analysis was conducted under steady-state flow and uniform-temperature conditions, and the isotropic linear-elastic formulation was used to compare the instantaneous structural responses of the different geometric configurations under

consistent loading conditions. Therefore, the present model does not account for transient thermal loads associated with cloud-induced solar-flux fluctuations, start-up and shutdown operations, or rapid temperature variations. These operating conditions may produce axial and through-wall temperature gradients and cyclic thermal stresses, which may modify the local stress distributions near the elbows, straight-to-elbow transition regions, and support locations [18,19]. Thermomechanical fatigue, time-dependent creep deformation and stress relaxation, and the long-term evolution of frictional constraints at the support clamps were also not considered. Repeated thermal cycles may result in fatigue accumulation at the identified high-stress locations, whereas time-dependent material and contact behavior, if relevant under the actual service conditions, may redistribute the local stresses [22]. Therefore, the identified high-stress locations should be interpreted as governing locations under the prescribed steady-state linear-elastic load cases rather than as definitive predictions of long-term damage. Transient thermal loading, fatigue, creep, and the evolution of support contact conditions require further investigation using time-dependent thermal–structural and material models.

2.4. Model Verification

The computational meshes for the fluid and structural domains are shown in Figure 4 Hexahedral-dominant meshes were generated for both computational domains using the MultiZone method, with local refinement applied to the elbows and the straight-to-elbow transition regions. Ten layers of boundary-layer mesh were established near the pipe wall, with a first-layer thickness of 0.75 mm and a growth rate of 1.2. Three elements were used through the pipe-wall thickness. Eight fluid-domain mesh sets and eight structural-domain mesh sets were generated to examine the sensitivity of the calculation results to the mesh size. The overall system resistance coefficient K_{sys} was used as the evaluation indicator for the fluid calculations, whereas the maximum total deformation and maximum von Mises equivalent stress under the combined load case with simplified internal pressure were used as the evaluation indicators for the structural calculations. Taking the result obtained using the eighth and finest mesh as the reference, the relative deviation of the response quantity corresponding to the ith mesh set was defined as

$$\Delta x = \left| \frac{x_i - x_{\text{ref}}}{x_{\text{ref}}} \right| \times 100\%$$

where x_i is the response quantity corresponding to the ith mesh set, and x_{ref} is the reference value corresponding to the eighth mesh set. The calculated results are listed in Tables 4 and 5.

Table 4. Fluid-domain mesh-independence test results.

Mesh Set	Number of Cells	K_{sys}	δK_{sys}/%
1	311,540	7.471	4.59
2	366,440	7.398	3.57
3	565,110	7.285	1.99
4	767,970	7.230	1.22
5	1,075,800	7.170	0.38
6	1,778,400	7.122	0.29
7	2,204,800	7.131	0.17
8	2,671,200	7.143	—

Table 4 shows that as the number of fluid-domain mesh cells increased from 311,540 to 2,671,200, K_{sys} decreased from 7.471 to 7.143. Mesh set 5 contained 1,075,800 cells, and the corresponding K_{sys} was 7.170, with a relative deviation of 0.38% compared with the reference value obtained from the finest mesh (set 8). Beyond mesh set 5, the marginal reduction in

the resistance coefficient diminished markedly. Considering both computational accuracy and cost, mesh set 5 of the fluid domain was adopted for the subsequent CFD simulations.

Table 5. Structural-domain mesh-independence test results.

Mesh Set	Number of Nodes	U_{comb}/mm	σ_{comb}/MPa	δU_{comb}/%	$\delta\sigma_{comb}$/%
1	367,950	140.09	209.93	0.08	0.55
2	497,530	139.98	212.09	0.00	1.59
3	695,800	140.00	210.76	0.01	0.95
4	833,400	139.96	209.57	0.01	0.38
5	1,018,100	140.00	208.72	0.01	0.03
6	1,636,500	139.97	208.80	0.01	0.01
7	2,488,800	139.93	208.83	0.04	0.02
8	3,993,100	139.98	208.78	—	—

Table 5 shows that as the number of structural-domain nodes increased from 367,950 to 3,993,100, the maximum total deformation stabilized around 139.98 mm, while the maximum von Mises equivalent stress gradually stabilized below 209 MPa. Mesh set 6 contained 1,636,500 nodes, yielding a maximum total deformation of 139.97 mm and a maximum von Mises equivalent stress of 208.80 MPa. Compared with the reference mesh (set 8), the relative deviations for both indicators were within 0.01%. Therefore, mesh set 6 was selected for the structural finite-element calculations.

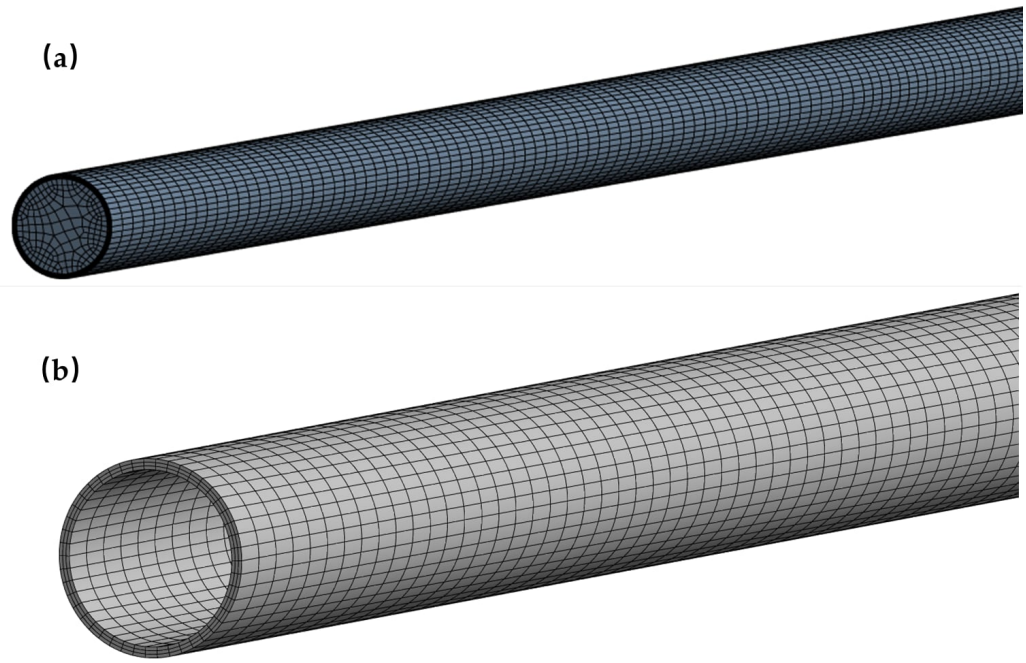


Figure 4. Schematic of the fluid and structural domain meshes: (**a**) fluid-domain mesh and near-wall boundary layers; (**b**) structural-domain mesh and mesh layers through the pipe-wall thickness.

Because publicly available experimental data corresponding to the full-scale molten-salt riser geometry and operating conditions considered in this study were not available, the results reported by Zhang et al. [6] were adopted for a benchmark-case comparison of the CFD calculation method. The validation model was established according to the pipe dimensions, bend angles, fluid properties, and boundary conditions reported by Zhang et al. [6]. The realizable $k-\varepsilon$ turbulence model, near-wall treatment method, and numerical discretization schemes were consistent with those used in the riser calculations

of the present study. Figure 5 compares the results obtained in the present study with those reported by Zhang et al. [6]. At an angle of 60°, the resistance coefficient calculated in the present study was 0.476, whereas the corresponding value reported by Zhang et al. was 0.431. The relative deviation was 10.44%, and the maximum deviation was 18.57%. For the different bend angles, the two sets of results exhibited the same trend, indicating the validity of the CFD setup used in this study.

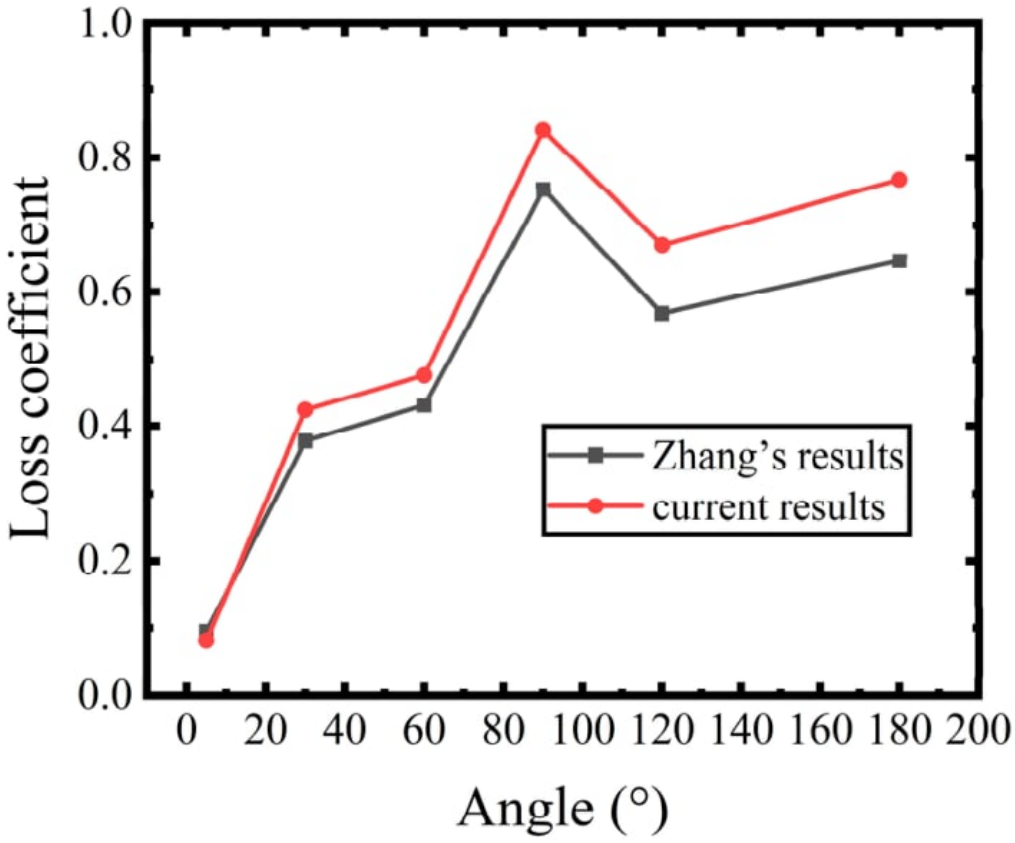


Figure 5. CFD validation results [6].

At present, no publicly available experimental or computational data are available for direct comparison with the complete CFD–FEA model under conditions consistent with the full-scale molten-salt riser considered in this study in terms of geometric configuration, operating conditions, load composition, and support configuration. Therefore, no direct comparison was performed for the complete CFD–FEA model. The structural calculation results were primarily used to compare the relative stress and deformation responses of different geometric configurations under consistent modeling conditions and were not used to determine the absolute prediction error of the actual riser structural response. The relevant conclusions are limited to the parameter ranges investigated in this study and are subject to the modeling assumptions of steady-state flow, constant molten-salt properties, linear-elastic material behavior, uniform temperature loading, and simplified support-and-hanger configurations.

3. Results and Discussion

3.1. Effect of Equivalent Inclined-Segment Length

The effects of different L_s/D_i values on the overall system resistance coefficient, maximum von Mises equivalent stress, and maximum total deformation were investigated, and the results are presented in Figure 6. As L_s/D_i increased from 10.695 to 26.471, K_{sys} con-

tinuously increased from 6.923 to 7.707, while the increment between adjacent calculation points gradually decreased from 0.247 to 0.116. These results indicate that increasing the length of the inclined pipe segment elevates the overall system resistance, with diminishing marginal increments. This behavior is mainly attributed to the continuous accumulation of frictional losses along the inclined pipe segment as its length increases. Meanwhile, the downstream flow-development distance after the elbow also increases, and the influence of the local disturbance induced by the elbow on the downstream flow is correspondingly reduced. Consequently, the increase in resistance becomes less pronounced with increasing equivalent inclined-segment length.

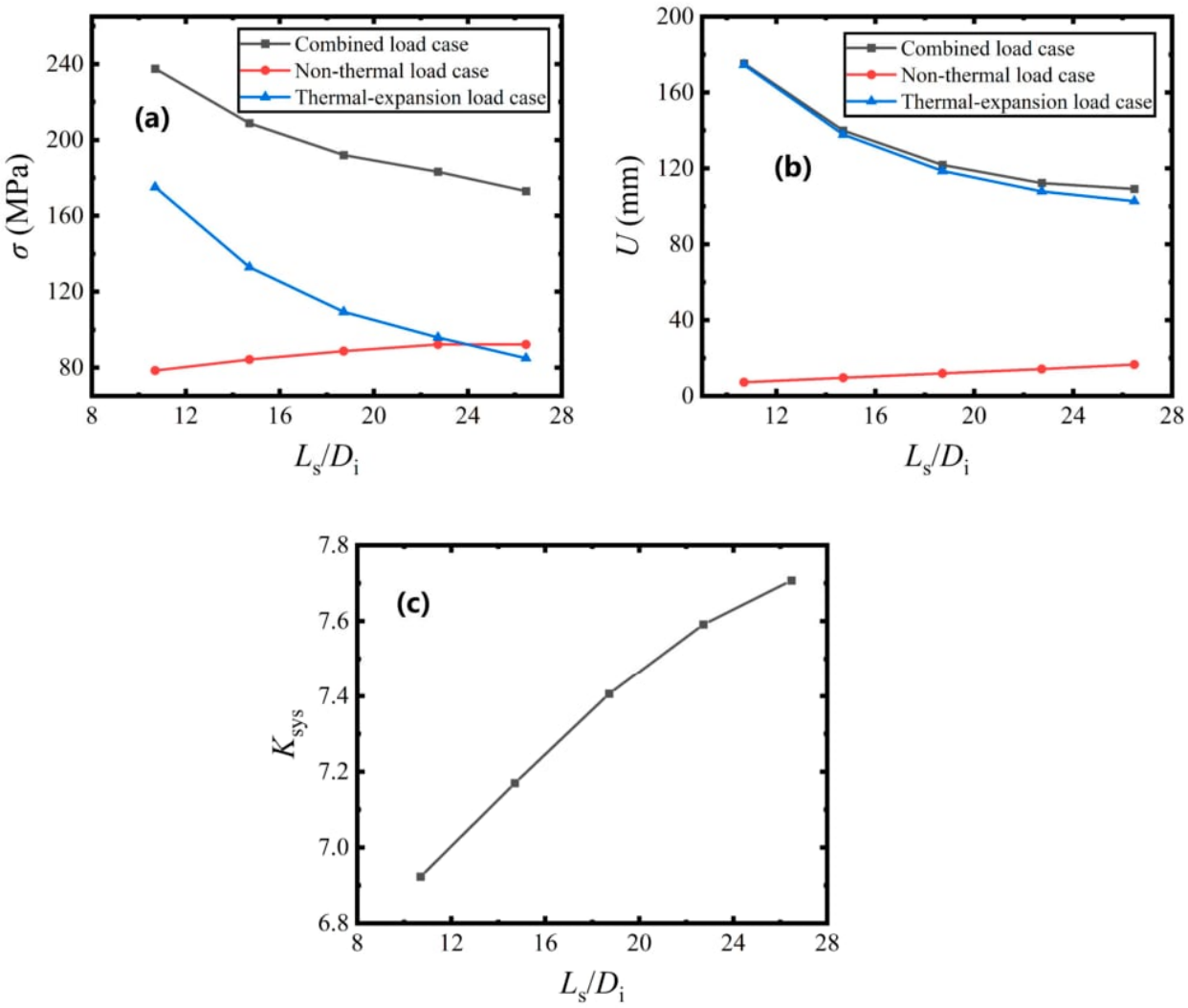


Figure 6. Hydraulic and structural responses under different equivalent inclined-segment lengths: (**a**) maximum von Mises equivalent stress; (**b**) maximum total deformation; (**c**) overall system resistance coefficient.

The structural responses exhibit trends different from those of the hydraulic response. Under the combined load case, σ_{comb} and U_{comb} decreased from 237.62 MPa and 175.34 mm to 173.06 MPa and 109.17 mm, respectively. The reductions under the thermal-expansion load case were greater, with σ_T and U_T decreasing from 175.19 MPa and 174.57 mm to 84.99 MPa and 102.72 mm, respectively. The calculation results indicate that extending the inclined pipe segment provides a longer deformation-accommodation path for thermal expansion. Thermal expansion can consequently be released progressively through more distributed bending and rotational deformation. This is considered to be the primary

reason for the pronounced reductions in the local thermal-expansion restraint and the corresponding peak stress and deformation. The non-thermal load case exhibited the opposite trend: σ_{NT} increased overall from 78.45 MPa to 92.20 MPa, while U_{NT} increased from 7.29 mm to 16.66 mm. This behavior is attributed to the change in the piping-system span caused by the increase in equivalent inclined-segment length, which strengthens the structural responses induced by self-weight, pressure, and support actions. Although the relative increase in U_{NT} is substantial, its absolute value remains considerably lower than the thermal-expansion deformation. Therefore, U_{comb} remains primarily controlled by thermal-expansion deformation over the entire parameter range.

Between $L_s/D_i = 22.727$ and 26.471, the maximum von Mises equivalent stresses under the thermal-expansion load case and the non-thermal load case intersect. This indicates that, with increasing equivalent inclined-segment length, the dominant contribution to the structural peak response shifts from the thermal-expansion effect to the non-thermal loading effect between $L_s/D_i = 22.727$ and 26.471. It should be noted that the maximum von Mises equivalent stress under the combined load case does not exhibit a simultaneous transition within this interval but continues to decrease. This is mainly because the locations of the peak stresses under different independent load cases are not necessarily identical. The equivalent stress under the combined load case is determined by the combined stress state resulting from the superposition of individual stress components. Therefore, a change in the ranking of the peak stresses under the independent load cases is not necessarily reflected directly in the peak stress under the combined load case.

3.2. Effect of Elbow Curvature Ratio

The effects of different R/D_i values on the overall system resistance coefficient and structural responses were investigated, and the results are presented in Figure 7. Figure 7c shows that, as R/D_i increased from 1.5 to 3.25, K_{sys} decreased successively from 7.525 to 7.364, 7.268, 7.203, and 7.170, corresponding to an overall reduction of 4.71%. The reduction in resistance between adjacent calculation points gradually decreased, indicating that increasing the elbow curvature ratio continuously reduces the overall system resistance, whereas its marginal resistance-reduction effect gradually weakens. This is because an increase in the curvature ratio distributes the change in the elbow centerline direction over a longer arc, resulting in a more gradual change in flow direction and a corresponding reduction in the additional flow losses induced by curvature. However, once the elbow has a relatively large curvature radius, further increases in R/D_i produce progressively limited improvements in resistance.

Figure 7a shows that σ under all three load cases decreased with increasing R/D_i. The reduction in σ_T was the largest, at approximately 23.27%, while σ_{NT} and σ_{comb} decreased by approximately 15.17% and 9.51%, respectively, when R/D_i increased from 1.50 to 3.25. This behavior is primarily related to the load-transfer mechanism in the elbow region. When the curvature radius is small, the change in flow direction is concentrated over a relatively short distance, resulting in more pronounced stress concentration in the straight-to-elbow transition region. As the curvature radius increases, deformation and load transfer are distributed over a larger arc, and the peak stress correspondingly decreases. It should be noted that the reduction under the thermal-expansion load case was substantially greater than those under the other two load cases. Within the parameter range considered in this study, the peak stress under the thermal-expansion load case exhibited a higher relative sensitivity to variations in the curvature ratio.

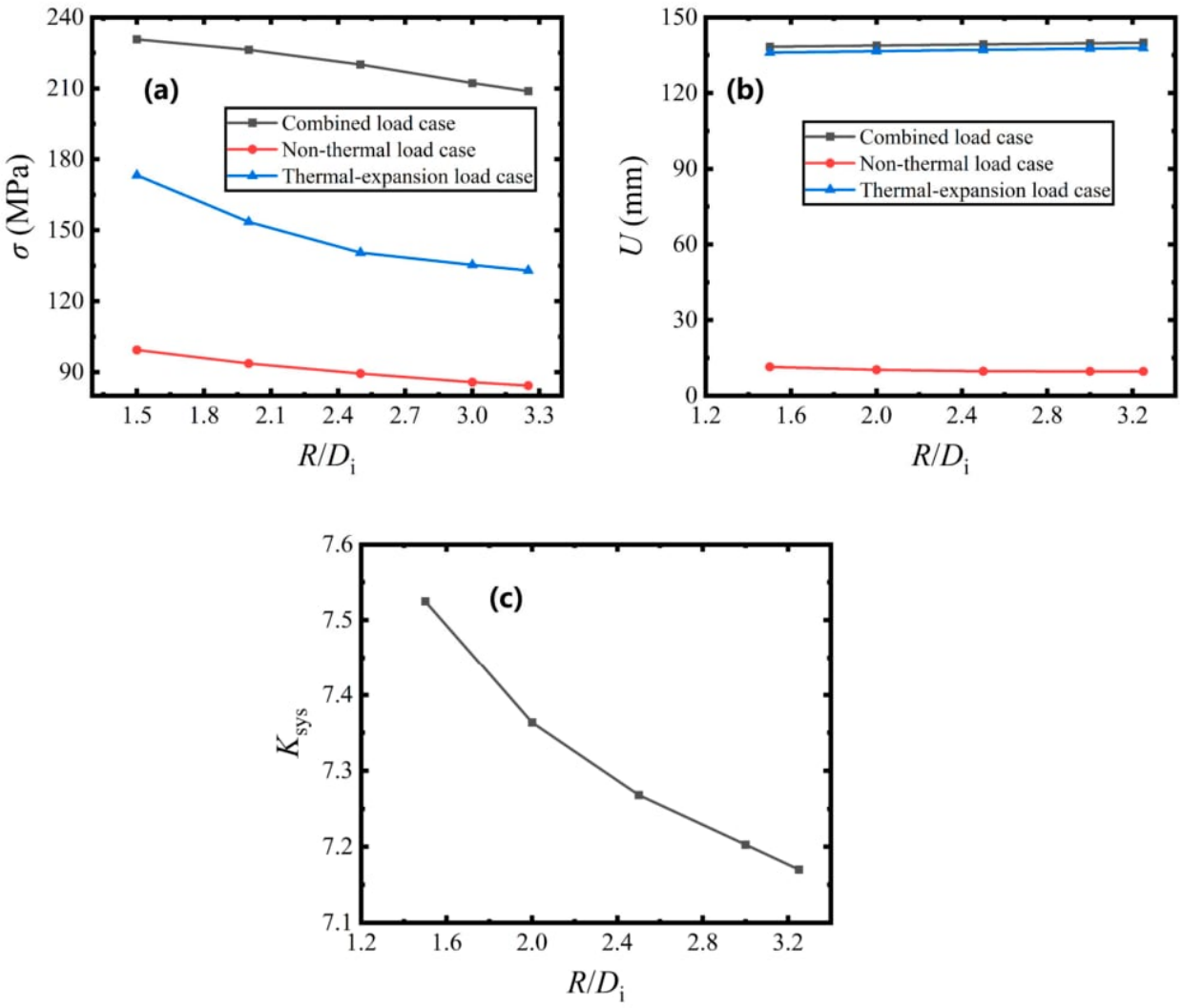


Figure 7. Hydraulic and structural responses under different elbow curvature ratios: (**a**) maximum von Mises equivalent stress; (**b**) maximum total deformation; (**c**) overall system resistance coefficient.

Figure 7b shows that the maximum total deformation was not sensitive to the curvature ratio. U_{comb} and U_T changed from 138.40 mm and 136.07 mm to 139.97 mm and 137.87 mm, respectively, corresponding to increases of 1.14% and 1.32%, respectively. U_{NT} decreased from 11.45 mm to 9.68 mm, and its absolute variation was also small. The deformation values under the two load cases remained close to each other, indicating that, for the piping-system layout considered in this study, the overall deformation was primarily controlled by thermal expansion. Although the elbow curvature radius significantly altered the local stress distribution, the principal thermal-deformation path remained essentially unchanged because the total height, inclined-segment angle, equivalent inclined-segment length, and support conditions were kept constant. Therefore, increasing the curvature ratio primarily reduced the local peak stress, while its influence on the overall deformation remained limited.

3.3. Effect of Inclined-Pipe Angle

Figure 8 presents the variation of the overall system resistance coefficient K_{sys} with inclined-segment angles θ. As θ increases from 30° to 45°, 60°, 75°, and 90°, K_{sys} rises monotonically from 6.522 to 8.765, corresponding to an overall increase of approximately 34.40%.

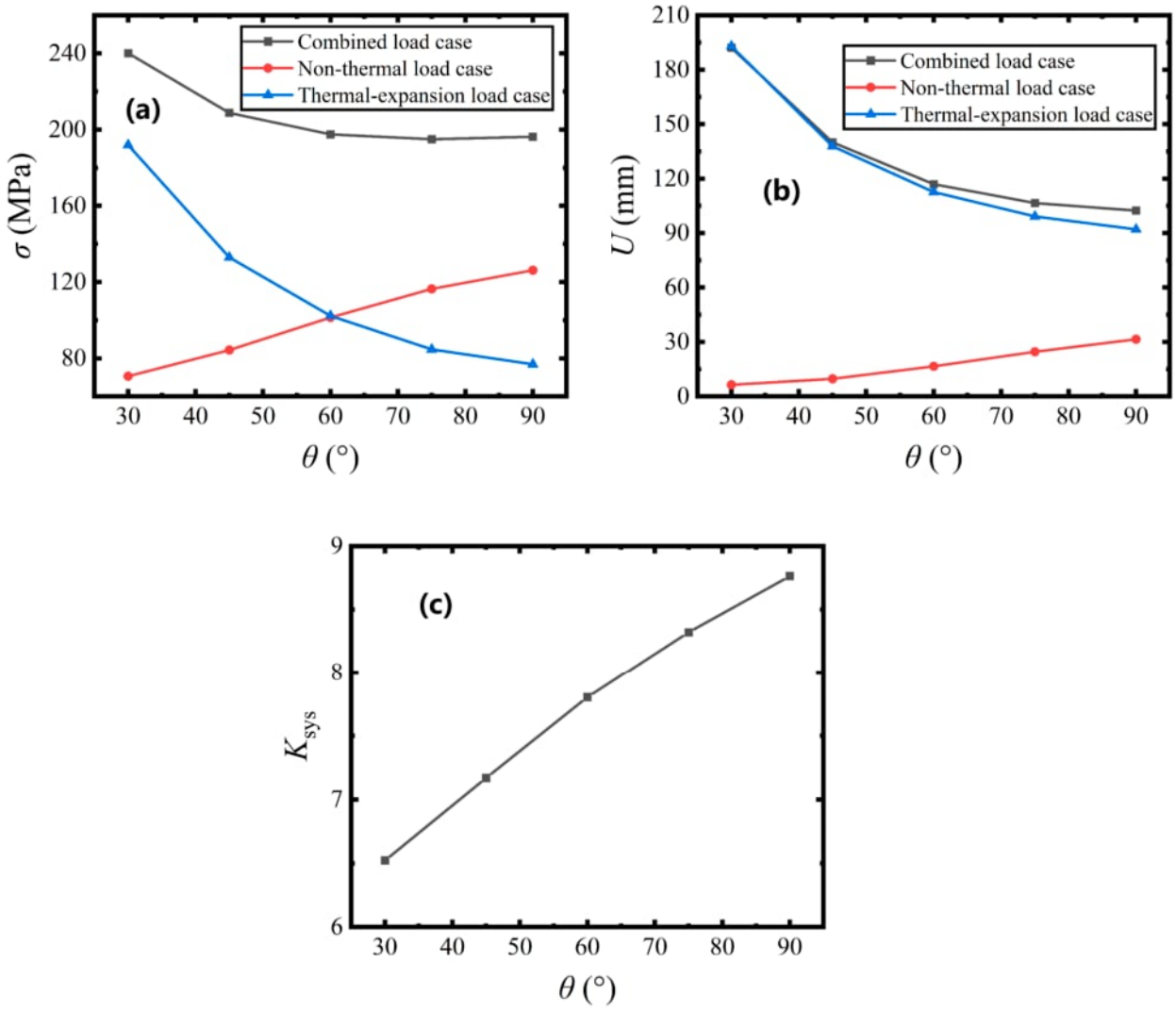


Figure 8. Hydraulic and structural responses under different inclined-segment angles: (**a**) maximum von Mises equivalent stress; (**b**) maximum total deformation; (**c**) overall system resistance coefficient.

The velocity distributions at the cross sections located 1*D*, 5*D*, 10*D*, and 20*D* downstream of the elbow outlet, as shown in Figure 9, indicate that significant velocity nonuniformity exists at the 1D downstream cross section for all θ values. The high-velocity region is displaced from the cross-sectional center, whereas the low-velocity region is concentrated on one side of the cross section. As the flow develops downstream to 5*D*, 10*D*, and 20*D*, the circumferential position and shape of the low-velocity region continue to change rather than simply recovering along a fixed orientation. The extent and distribution of the low-velocity region also differ considerably among the different θ values.

Figure 10 presents the velocity magnitude along representative streamlines within the typical return-bend section for different inclined-segment angles. The horizontal coordinate represents the normalized cumulative streamline distance, extending from $10D_i$ upstream of the first elbow inlet to $20D_i$ downstream of the typical section outlet. The shaded regions indicate the four elbows. The velocity magnitude exhibits pronounced local fluctuations within or near the elbows, whereas smoother variations generally occur along the connecting pipe segments. For the 30° configuration, a pronounced velocity reduction occurs near the third elbow, while for 45°, the deepest velocity minimum appears near the fourth elbow. For 60° and 75°, substantial velocity reductions occur near the second and third elbows. For 90°, pronounced velocity reductions occur near the first, second, and third elbows. In

several configurations, the velocity recovers downstream of the local minima, although the extent and rate of recovery differ.

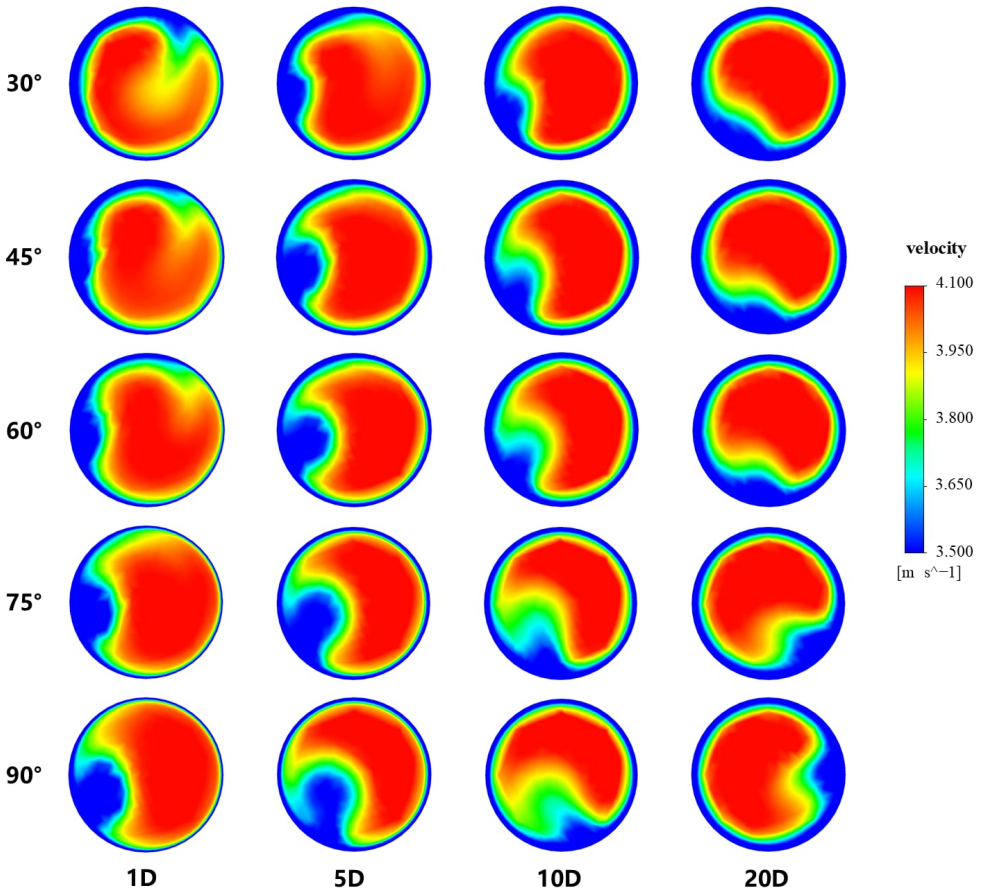


Figure 9. Velocity distributions at representative cross sections downstream of the elbow under different inclined-segment angles: the rows correspond to $\theta = 30°$, 45°, 60°, 75°, and 90°, respectively; the columns correspond to the cross sections located at 1*D*, 5*D*, 10*D*, and 20*D* downstream of the elbow outlet, respectively.

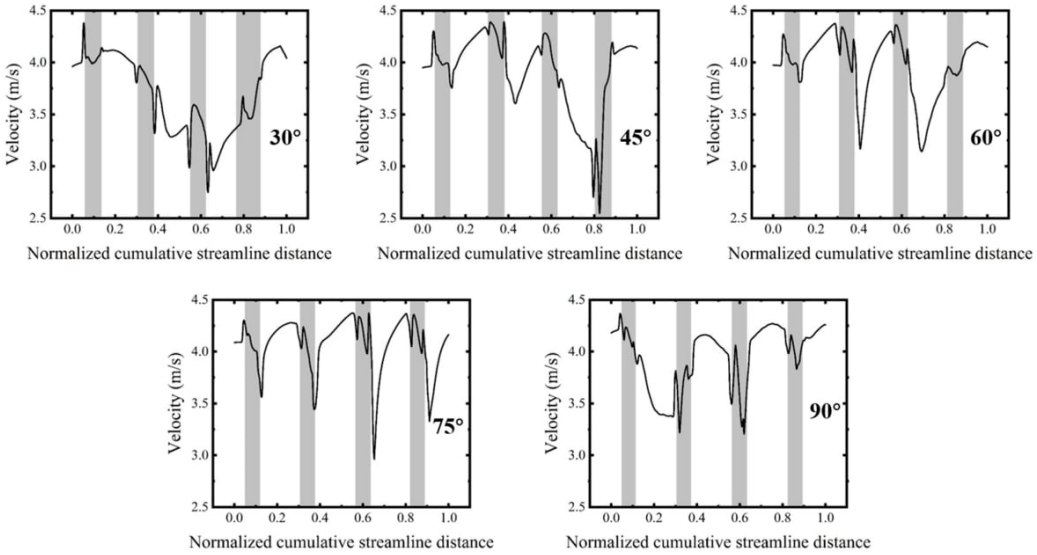


Figure 10. Velocity magnitude along representative streamlines through the typical section for $\theta = 30°$, 45°, 60°, 75°, and 90°.

The turbulent kinetic energy distributions in Figure 11 show that the regions of high turbulent kinetic energy are primarily concentrated in the elbow and the adjacent flow-turning regions, with their locations and distribution ranges shifting along the elbow geometry as θ increases. The aforementioned velocity nonuniformity and local enhancement of turbulent fluctuations collectively indicate that increasing θ intensifies flow deflection and additional turbulent dissipation in the bending region, thereby causing a continuous rise in K_{sys}.

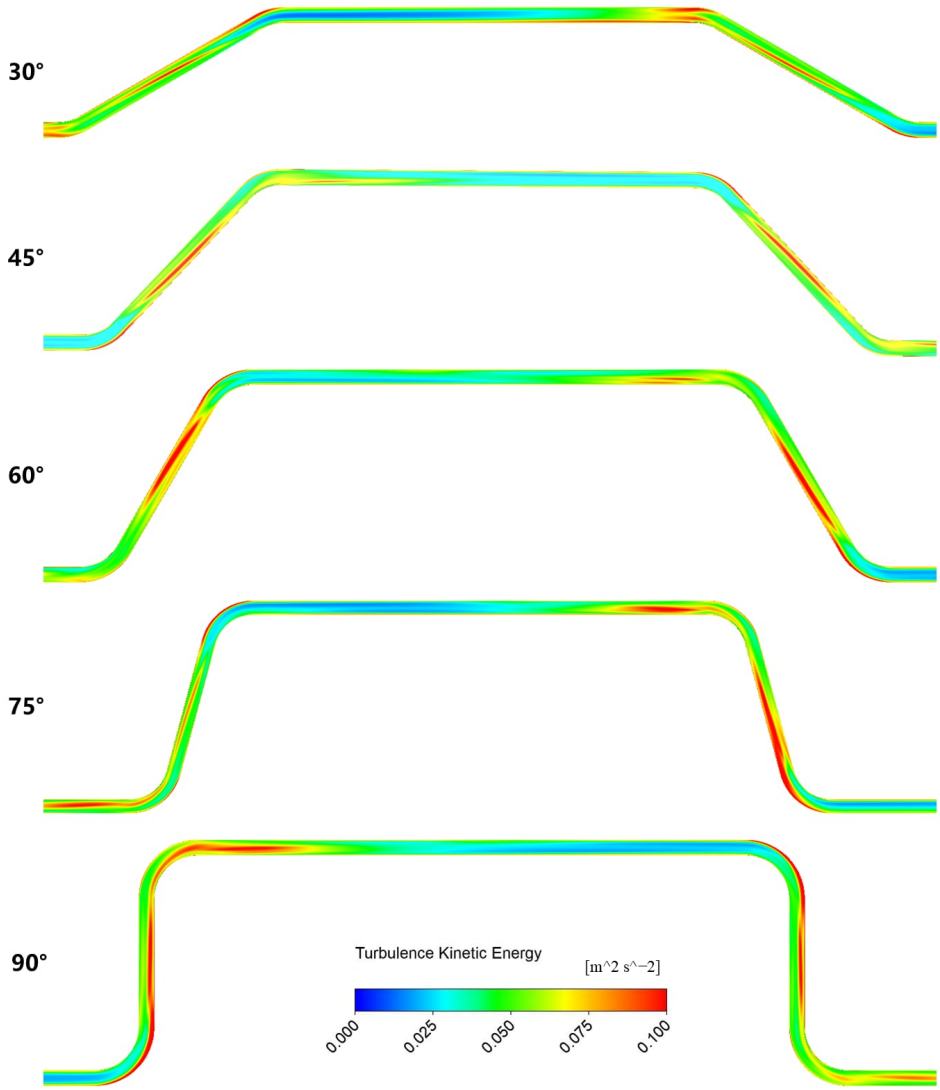


Figure 11. Turbulent kinetic energy distributions under different inclined-segment angles: from top to bottom, the configurations correspond to θ = 30°, 45°, 60°, 75°, and 90°, respectively.

The structural responses exhibit trends different from those of the hydraulic response as θ varies. The values of σ_{comb} at θ = 30°, 45°, 60°, 75°, and 90° were 240.15, 208.80, 197.54, 194.95, and 196.26 MPa, respectively, showing an initial decrease followed by a slight increase. In contrast, U_{comb} decreased from 192.13 mm at θ = 30° to 102.37 mm at θ = 90°. The deformation contours in Figure 12 show that the regions associated with relatively large total deformation were primarily located near the lower elbows of the successive return-bend units. The maximum total deformation of the entire riser occurred in the first return-bend unit for the investigated angle levels. The numerical results indicate that increasing θ changes the spatial distribution of total deformation and reduces the combined-load maximum total deformation within the investigated range.

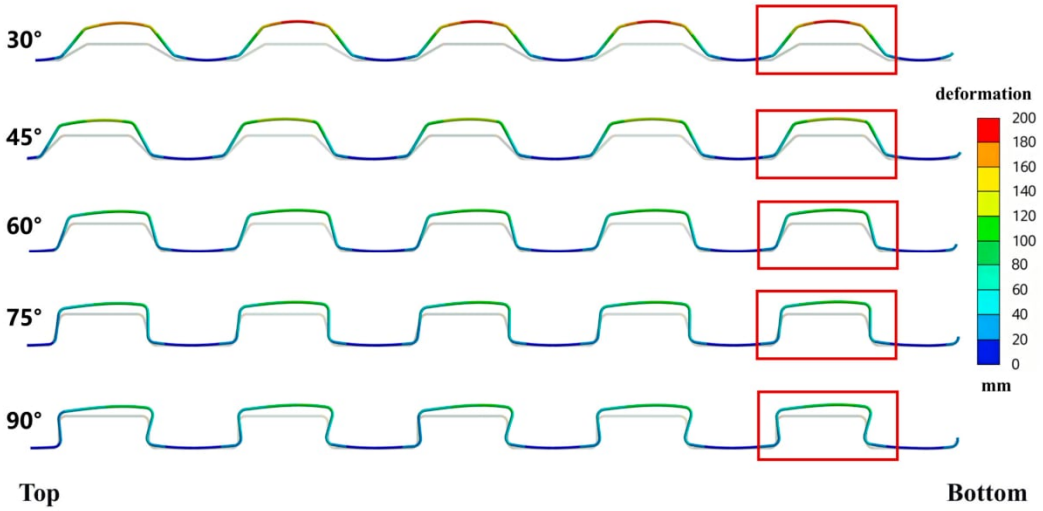


Figure 12. Deformation distributions under the combined load case for different inclined-segment angles: from top to bottom, the configurations correspond to $\theta = 30°$, 45°, 60°, 75°, and 90°, respectively; the red boxes indicate the locations of the maximum total deformation in the entire riser.

The two load cases exhibited opposite responses to variations in θ. As θ increased, σ_{NT} continuously increased from 70.58 MPa to 126.22 MPa, while U_{NT} increased from 6.39 mm to 31.47 mm. In contrast, σ_T continuously decreased from 191.90 MPa to 76.84 MPa, and U_T decreased from 192.94 mm to 92.06 mm. The two stress–response curves intersected between 60° and 75°. These results indicate that increasing the inclined-segment angle improves the release of thermal expansion deformation in the piping system, thereby continuously reducing the stress and deformation associated with thermal expansion. At the same time, it modifies the load-carrying path under the effects of self-weight, pressure, and support reactions, resulting in a gradual increase in the stress induced by non-thermal loads.

It should be noted that, although the relative magnitudes of the maximum von Mises equivalent stresses under the non-thermal load case and the thermal-expansion load case changed between 60° and 75°, σ_{comb} did not undergo a simultaneous transition. Instead, it decreased from 208.80 MPa at 45° to 197.54 MPa at 60°, decreased further to 194.95 MPa at 75°, and then increased slightly to 196.26 MPa at 90°. Figure 13 presents the stress distributions under the non-thermal load case and the thermal-expansion load case for the representative 30° and 90° configurations. Under both load cases, the high-stress regions were primarily located at the elbows and the straight-to-elbow transition regions. However, as the configuration changed, the governing locations corresponding to the peak stresses shifted, while the distribution ranges and orientations of the high-stress regions also changed. Under the non-thermal load case, the maximum von Mises equivalent stress generally increased with increasing angle. Under the thermal-expansion load case, however, the peak stress decreased substantially, accompanied by a redistribution of the governing locations. These results demonstrate that the variation in σ_{comb} cannot be determined directly from the relative magnitudes of the maximum stresses under the two independent load cases. Instead, it is jointly related to the local stress state and its spatial distribution resulting from the non-thermal and thermal-expansion loads.

Within the range of 30° to 75°, the overall stress level in the region controlled by the combined load case continuously decreased. When the angle was further increased to 90°, the non-thermal-load response continued to increase, whereas the stress-reduction effect under the thermal-expansion load case was substantially weakened. Combined with the redistribution of the local high-stress regions, these effects ultimately caused the maximum von Mises equivalent stress under the combined load case to increase slightly from 194.95 MPa at 75° to 196.26 MPa at 90°.

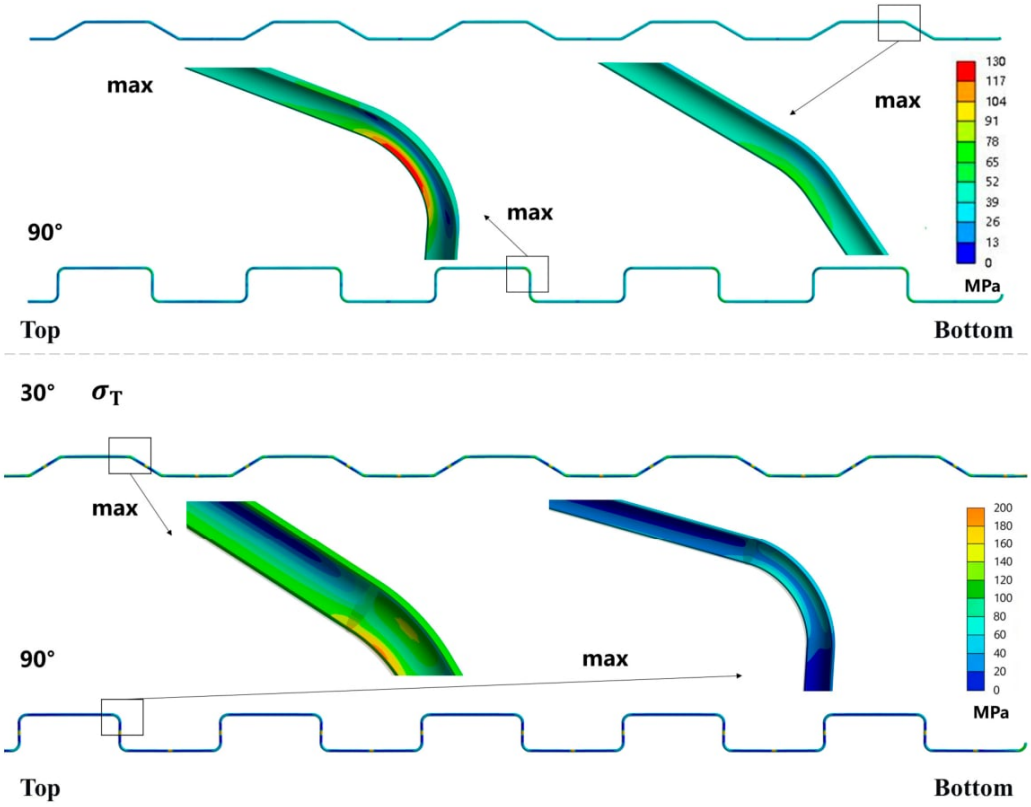


Figure 13. Stress distributions and corresponding peak-stress locations under the non-thermal load case and thermal-expansion load case for representative inclined-segment angle configurations.

3.4. Cross-Parameter Comparison and Engineering Implications

3.4.1. Correlations Between Hydraulic and Combined-Load Structural Responses

Figure 14a–c show the corresponding relationships between the maximum von Mises equivalent stress under the combined load case, σ_{comb}, and the overall system resistance coefficient, K_{sys}, as the three geometric parameters vary. The three data sets exhibit distinctly different response paths in the same K_{sys}–σ_{comb} plane. Variations in the elbow curvature ratio correspond to an approximately concurrent response. As the configuration changes from a smaller to a larger curvature ratio, both K_{sys} and σ_{comb} shift toward lower levels, indicating that this parameter does not produce a pronounced hydraulic–stress conflict within the range investigated in this study. In contrast, the equivalent inclined-segment length exhibits an opposite relationship: an increase in K_{sys} is accompanied by a continuous decrease in σ_{comb}, indicating that the improvement in structural stress performance is achieved at the expense of additional hydraulic loss.

The response path associated with the inclined-segment angle differs from those associated with the other two parameters. As θ increases, K_{sys} continuously increases, whereas σ_{comb} decreases from 240.15 MPa to 194.95 MPa at the 75° configuration and subsequently increases to 196.26 MPa at the 90° configuration. Therefore, the range of 30–75° represents a reduction in peak stress at the cost of increased resistance. When the angle is further increased beyond 75°, the resistance continues to increase, whereas the maximum stress no longer improves. The turning point shown in Figure 14b indicates that the vicinity of 75° corresponds to the point within the current discrete-angle range at which the continuously increasing hydraulic penalty is accompanied by a change in the structural-stress benefit. This behavior does not conform to a simple monotonic trade-off relationship.

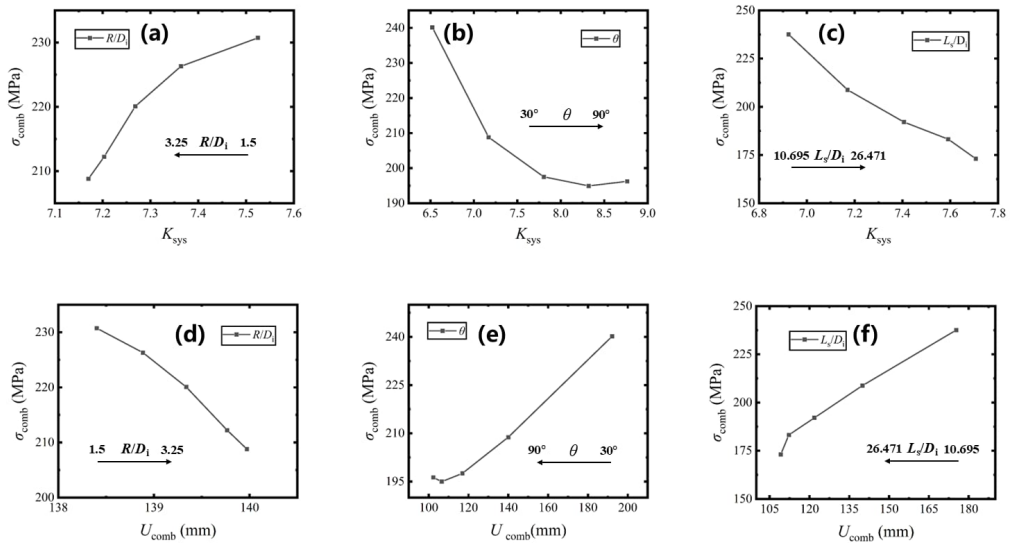


Figure 14. Correlations between hydraulic and combined-load structural responses under different geometric parameters: (**a**) relationship between σ_{comb} and K_{sys} for varying R/D_i; (**b**) relationship between σ_{comb} and K_{sys} for varying θ; (**c**) relationship between σ_{comb} and K_{sys} for varying L_s/D_i; (**d**) relationship between σ_{comb} and U_{comb} for varying R/D_i; (**e**) relationship between σ_{comb} and U_{comb} for varying θ; (**f**) relationship between σ_{comb} and U_{comb} for varying Ls/D_i.

Figure 14d–f further illustrate the relationships between σ_{comb} and the maximum total deformation under the combined load case, U_{comb}. As the elbow curvature ratio varies, U_{comb} remains within a narrow range of approximately 138.40–139.97 mm, whereas σ_{comb} varies by 21.94 MPa. This indicates that the elbow curvature ratio primarily changes the peak stress level and has a relatively limited influence on the maximum total deformation. As the equivalent inclined-segment length varies, σ_{comb} and U_{comb} decrease simultaneously, indicating that extending the inclined pipe segment changes both the peak stress and the overall deformation level. The response to the inclined-segment angle exhibits a turning-point behavior: both stress and deformation decrease concurrently within the range of 30–75°, whereas within the range of 75–90°, the deformation continues to decrease while the stress begins to increase slightly. Accordingly, the continuous decrease in maximum total deformation does not directly indicate a continuous improvement in peak stress, particularly for configurations with relatively large inclined-segment angles, where the two structural indicators exhibit response separation.

3.4.2. Relative Response Variations from the Baseline Configuration

The geometric parameters of the common baseline configuration were $L_s/D_i = 14.706$, $R/D_i = 3.25$, and $\theta = 45°$, corresponding to $K_{sys} = 7.170$, $\sigma_{comb} = 208.80$ MPa, $U_{comb} = 139.97$ mm, and $m_{pipe} = 48{,}508$ kg. The response variation of each configuration relative to the baseline configuration was calculated as follows:

$$\Delta X = \frac{X - X_0}{X_0} \times 100\%$$

The relative variations of each configuration are listed in Table 6.

Table 6 shows that, as R/D_i increased from 1.50 to 3.25, K_{sys} and σ_{comb} continuously decreased. Relative to the baseline configuration, K_{sys} and σ_{comb} at $R/D_i = 1.50$ increased by 4.95% and 10.51%, respectively, indicating that σ_{comb} was more responsive to variations in the curvature ratio within the parameter range investigated in this study. U_{comb} increased slightly with increasing R/D_i, with a maximum increase of 1.12%, whereas m_{pipe} decreased slightly, with a maximum reduction of no more than 0.32%. Therefore, increasing the elbow

curvature ratio can simultaneously reduce the overall system resistance, peak stress, and pipe mass, while causing only a slight increase in deformation under the combined load case. Overall, the elbow curvature ratio primarily affects the overall system resistance and peak stress, while exerting a relatively limited influence on the maximum total deformation and steel material usage.

Table 6. Relative variations in hydraulic response, structural response, and pipe mass of each single-factor configuration with respect to the baseline configuration.

Parameter	Parameter Level	ΔK_{sys}/%	$\Delta \sigma_{comb}$/%	ΔU_{comb}/%	Δm_{pipe}/%
L_s/D_i	10.695	−3.45	+13.80	+25.26	−2.52
	14.706 (Baseline)	0.00	0.00	0.00	0.00
	18.717	+3.30	−8.01	−12.94	+2.52
	22.727	+5.88	−12.25	−19.80	+5.04
	26.471	+7.49	−17.12	−22.01	+7.40
R/D_i	1.50	+4.95	+10.51	−1.12	+0.32
	2.00	+2.70	+8.39	−0.78	+0.23
	2.50	+1.37	+5.40	−0.45	+0.14
	3.00	+0.46	+1.64	−0.15	+0.05
	3.25 (Baseline)	0.00	0.00	0.00	0.00
θ	30	−9.04	+15.01	+37.26	−4.59
	45 (Baseline)	0.00	0.00	0.00	0.00
	60	+8.84	−5.39	−16.44	+5.64
	75	+16.06	−6.63	−23.86	+11.61
	90	+22.24	−6.00	−26.87	+16.94

The multi-indicator response associated with variations in the inclined-segment angle is more pronounced. Compared with the 45° baseline configuration, the pipe mass and K_{sys} of the 30° configuration decreased by 4.59% and 9.04%, respectively, whereas σ_{comb} and U_{comb} increased by 15.01% and 37.26%, respectively. This indicates that reducing the inclined-segment angle decreases the steel material usage and overall system resistance, but simultaneously increases the structural response. When the angle increased to 60° and 75°, the pipe mass increased by 5.64% and 11.61%, respectively, and K_{sys} increased by 8.84% and 16.06%, respectively, whereas σ_{comb} decreased by 5.39% and 6.63%, respectively, and U_{comb} decreased by 16.44% and 23.86%, respectively. When the angle was further increased to 90°, the increases in pipe mass and resistance expanded to 16.94% and 22.24%, respectively, and the reduction in maximum total deformation reached 26.87%. However, the reduction in maximum stress decreased from 6.63% at 75° to 6.00% at 90°. Therefore, a larger inclined-segment angle can continue to reduce the maximum total deformation, but it requires additional pipe material and causes greater hydraulic loss; moreover, σ_{comb} does not continuously decrease with increasing angle. Within the discrete angle range investigated in this study, the 45° configuration reduced the maximum stress and maximum total deformation relative to the 30° configuration, while exhibiting lower pipe mass and overall system resistance than the 60°, 75° and 90° configurations. Thus, it demonstrates a degree of coordination among hydraulic performance, structural response, and pipe material usage.

The equivalent inclined-segment length exhibits a different variation trend relative to the baseline value. When L_s/D_i decreased to 10.695, the pipe mass and K_{sys} decreased by 2.52% and 3.45%, respectively, whereas σ_{comb} and U_{comb} increased by 13.80% and 25.26%, respectively. When L_s/D_i increased to 18.717, 22.727, and 26.471, the pipe mass increased by 2.52%, 5.04%, and 7.40%, respectively. The corresponding increases in resistance were 3.30%, 5.88%, and 7.49%, while the reductions in maximum stress increased to 8.01%, 12.25%, and 17.12%, respectively, and the reductions in maximum total deformation increased to 12.94%,

19.80%, and 22.01%, respectively. These results indicate that increasing the equivalent inclined-segment length reduces the maximum stress and maximum total deformation, but simultaneously increases the steel material usage and overall system resistance. In particular, when L_s/D_i increased from 22.727 to 26.471, the pipe mass increased by an additional 2.24%, and the reduction in maximum stress relative to the baseline configuration increased by a further 4.87 percentage points, whereas the reduction in maximum total deformation increased by only 2.21 percentage points. This indicates that the improvement in deformation within this interval became less pronounced, whereas the stress continued to decrease.

The single-factor parametric design adopted in this study identifies the individual response trends of L_s/D_i, R/D_i, and θ, but does not account for potential interactions among them. Future work may employ response surface methodology and multi-objective optimization to investigate multi-parameter coupling and the trade-offs among hydraulic performance, structural response, and pipe material usage.

3.5. Engineering Design Recommendations

Based on the preceding comparisons of hydraulic performance, structural response, and pipe mass, the parameter-specific response trends can provide a basis for the hierarchical selection of molten-salt riser configurations within the investigated parameter ranges. Provided that the lateral-layout space requirements are satisfied, priority may be given to increasing the elbow curvature ratio. As this parameter increases, the overall system resistance and the maximum von Mises equivalent stress under the combined load case decrease simultaneously, while the variations in pipe mass and maximum total deformation remain within 0.32% and 1.12%, respectively. Therefore, increasing the elbow curvature ratio can improve the hydraulic performance and reduce the peak stress without significantly increasing the steel material usage.

The equivalent inclined-segment length and inclined-segment angle can be used to further regulate the structural response, but their values should be constrained by the overall system resistance and pipe material usage. Increasing the equivalent inclined-segment length can reduce the maximum von Mises equivalent stress and maximum total deformation under the combined load case, but it also increases the overall system resistance and pipe mass. Moreover, the reduction in maximum total deformation becomes less pronounced within the range of larger length-to-diameter ratios. Increasing the inclined-segment angle produces a relatively sustained reduction in maximum total deformation, but the overall system resistance and pipe mass also increase, and the maximum von Mises equivalent stress under the combined load case increases after 75°. Therefore, neither parameter should be continuously increased based on a single structural indicator. Instead, both parameters should be selected jointly according to the allowable stress, allowable deformation, overall system resistance, and material usage.

With respect to the inclined-segment angle, the 45° configuration reduces the maximum von Mises equivalent stress and maximum total deformation under the combined load case relative to the 30° configuration, while exhibiting lower overall system resistance and pipe mass than the 60°, 75° and 90° configurations. Overall, provided that the stress and deformation satisfy the engineering design limits, 45° can be considered a candidate angle that balances hydraulic performance, structural response, and pipe material usage.

The component-level implications of the present results can also be considered within the wider context of solar thermal integration into power-generation systems. Cutuli et al. showed that different strategies for integrating solar energy with biomass and natural gas combined cycles lead to different overall efficiencies and renewable-energy contributions [27]. For tower-based systems retaining a molten-salt receiver-to-TES loop, the

hydraulic resistance and structural constraints of the thermal-transport components should therefore be considered together with the system-level integration requirements.

4. Conclusions

A full-scale molten-salt riser model was established under fixed total-height and lateral-space constraints to investigate the effects of the inclined-segment length-to-diameter ratio, elbow curvature ratio, and inclined-segment angle on the hydraulic performance, structural response, and pipe mass of the system. The main conclusions are as follows:

(1) As L_s/D_i increased, K_{sys} continuously increased, whereas the maximum von Mises equivalent stress and maximum total deformation under the combined load case continuously decreased. The maximum von Mises equivalent stress under the non-thermal load case increased overall, while that under the thermal-expansion load case continuously decreased. The two response curves intersected between the two calculation points at $L_s/D_i = 22.727$ and 26.471, indicating a transition in the relative stress levels of the two independent load cases with increasing equivalent inclined-segment length.

(2) As R/D_i increased, K_{sys} and the maximum von Mises equivalent stress under the combined load case continuously decreased, whereas the maximum total deformation under the combined load case varied only slightly. The maximum von Mises equivalent stresses under the non-thermal load case and the thermal-expansion load case both remained on a decreasing trend. Variations in the elbow curvature ratio were primarily reflected in the overall system resistance and peak stress levels.

(3) As θ increased, K_{sys} continuously increased, whereas the maximum total deformation under the combined load case continuously decreased. The maximum von Mises equivalent stress under the combined load case reached the minimum value among the five discrete configurations at 75° and then increased slightly at 90°. The maximum von Mises equivalent stresses under the non-thermal load case and the thermal-expansion load case exhibited opposite trends, and their two response curves intersected between the calculation points at 60° and 75°. The stress results also show that the locations of the maximum von Mises stress changed with θ. The velocity and turbulent kinetic energy distributions at the cross sections downstream of the elbow also changed substantially with the angle.

(4) The three geometric parameters did not produce consistent effects on the hydraulic performance, structural response, and pipe mass. Increasing the equivalent inclined-segment length increased the overall system resistance and pipe mass, while reducing the maximum stress and maximum total deformation. Increasing the elbow curvature ratio simultaneously reduced the overall system resistance and maximum stress with little change in pipe mass. Although increasing the inclined-segment angle continuously reduced the maximum total deformation, it increased the overall system resistance and pipe mass, while the maximum stress exhibited a nonmonotonic variation. Among the five discrete angle configurations investigated, the 45° configuration exhibited lower maximum stress and maximum total deformation than the 30° configuration, as well as lower overall system resistance and pipe mass than the 60°, 75° and 90° configurations. Accordingly, the 45° configuration demonstrated a degree of coordination among hydraulic performance, structural response, and pipe material usage.

Author Contributions: Conceptualization, Y.L.; methodology, Y.L. and J.Q.; software, Z.Y. and Z.W.; validation, Z.W. and X.L.; formal analysis, J.X. and Z.Y.; investigation, Y.L. and Z.Y.; resources, Y.L. and Z.W.; data curation, Z.Y., Y.L. and X.L.; writing—original draft preparation, Y.L.; writing—review and editing, Z.Y., J.Q. and Z.W.; visualization, J.Q. and Z.Y.; supervision, Y.L. and Z.W.; project

administration, J.X., X.L. and Z.W.; funding acquisition, Y.L. and Z.W. All authors have read and agreed to the published version of the manuscript.

Funding: This research was funded by the Research and Development Program of State Power Investment Corporation Limited (SPIC), China (Grant No. 37-K2025-103).

Data Availability Statement: The original contributions presented in this study are included in the article. Further inquiries can be directed to the corresponding author.

Conflicts of Interest: Authors Yida Liu, Jinsheng Qi, Xiaoliang Li, and Junxiang Xu were employed by the company Shandong Electric Power Engineering Consulting Institute Co., Ltd. (a subsidiary of State Power Investment Corporation). The remaining authors, Zijiang Yang and Zhan Wang, are from Shandong University and declare that the research was conducted in the absence of any commercial or financial relationships that could be construed as potential conflicts of interest. The authors declare that this study received funding from State Power Investment Corporation (China). As employees of its subsidiary, the aforementioned authors were involved in the study design, data collection, analysis, interpretation of data, and the writing of this article.

Abbreviations

Symbol	Description	Unit
H_{total}	Total height of the piping system	m
D_{i}	Internal diameter of the pipe	mm
D_{o}	External diameter of the pipe	mm
D	Characteristic length used to denote the downstream cross-sectional locations; $D = D_{\text{i}}$ in this study	mm
R	Radius of curvature along the elbow centerline	mm
R/D_{i}	Elbow curvature ratio	—
L_{s}	Length of the inclined pipe segment centerline	mm
$L_{\text{s}}/D_{\text{i}}$	Equivalent Inclined-Segment Length; Inclined-segment length-to-diameter ratio	—
θ	Inclination angle of the inclined pipe segment centerline relative to the vertical direction	°
ρ	Molten-salt density	$\text{kg}\cdot\text{m}^{-3}$
μ	Dynamic viscosity of molten salt	Pa·s
$\boldsymbol{u}$	Velocity vector	$\text{m}\cdot\text{s}^{-1}$
p	Pressure	Pa
$\boldsymbol{g}$	Gravitational acceleration vector	$\text{m}\cdot\text{s}^{-2}$
v	Cross-sectional average velocity in the pipe	$\text{m}\cdot\text{s}^{-1}$
m_{pipe}	Pipe mass	kg
Δp_{sys}	Pressure loss between the system inlet and outlet	Pa
K_{sys}	Overall system resistance coefficient	—
σ	Maximum von Mises equivalent stress	MPa
U	Maximum total deformation	mm
σ_{comb}	Maximum von Mises equivalent stress under the combined load case	MPa
U_{comb}	Maximum total deformation under the combined load case	mm
σ_{T}	Maximum von Mises equivalent stress under the thermal-expansion load case	MPa
U_{T}	Maximum total deformation under the thermal-expansion load case	mm
σ_{NT}	Maximum von Mises equivalent stress under the non-thermal load case	MPa
U_{NT}	Maximum total deformation under the non-thermal load case	mm
x_i	Response quantity corresponding to the ith mesh group	Same as the corresponding response quantity
x_{ref}	Reference response quantity corresponding to the eighth and finest mesh group	Same as the corresponding response quantity
δ_x	Relative deviation of the response quantity for the ith mesh group from that of the reference mesh	%
X	Response quantity to be compared	Same as the corresponding response quantity
X_0	Response quantity corresponding to the baseline configuration	Same as the corresponding response quantity
ΔX	Relative variation in the response quantity with respect to the baseline configuration	%

References

1. Gonzalez-Roubaud, E.; Perez-Osorio, D.; Prieto, C. Review of commercial thermal energy storage in concentrated solar power. *Renew. Sustain. Energy Rev.* **2017**, *80*, 133–148. [CrossRef]
2. Cristaudo, A.; Nicoletti, F.; Rovense, F.; Gaggioli, W.; Ferraro, V.; Arcuri, N. Concentrated solar thermal integrated with a novel dual-rock bed thermal energy storage for solar industrial process heat: Energy and economic analysis. *Sustain. Energy Technol. Assess.* **2026**, *88*, 104920. [CrossRef]
3. Frantz, C.; Binder, M.; Busch, K.; Ebert, M.; Heinrich, A.; Kaczmarkiewicz, N.; Schlögl-Knothe, B.; Kunze, T.; Schuhbauer, C.; Stetka, M.; et al. Basic engineering of a high performance molten salt tower receiver system. *AIP Conf. Proc.* **2022**, *2445*, 110002. [CrossRef]
4. Itō, H. Pressure losses in smooth pipe bends. *J. Basic Eng.* **1960**, *82*, 131–140. [CrossRef]
5. Idelchik, I.E. *Handbook of Hydraulic Resistance*; U.S. Atomic Energy Commission: Washington, DC, USA, 1966.
6. Zhang, J.; Wang, D.; Wang, W.; Zhu, Z. Numerical investigation and optimization of the flow characteristics of bend pipe with different bending angles. *Processes* **2022**, *10*, 1510. [CrossRef]
7. Du, X.; Wei, A.; Fang, Y.; Yang, Z.; Wei, D.; Lin, C.-H.; Jin, Z. The effect of bend angle on pressure drop and flow behavior in a corrugated duct. *Acta Mech.* **2020**, *231*, 3755–3777. [CrossRef]
8. Helmizar, H.; Nopita, D.; Witanto, Y.; Shai, K.; Putra, R.D.E.; Mainil, A.K. Computational fluid dynamics study on head loss through 90° elbows with curvature radius variation. *Int. J. Eng. Trans. C Asp.* **2026**, *39*, 1438–1452. [CrossRef]
9. Khan, M.; Haque, J.; Putul, L.; Sohel, S.H. Thermal hydraulic analysis of turbulent flow of superheated steam through multiple configurations of 3D angular piping bend in power plant installations. *J. Therm. Sci. Eng. Appl.* **2024**, *16*, 061003. [CrossRef]
10. Khan, M.M.H.; Haque, J.; Islam, S.; Putul, L.K.; Hassan, M. Effect of variable angular piping bends geometry on turbulent flow of supercritical water in an SCWR plant piping network: A three-dimensional computational fluid dynamics investigation. *J. Nucl. Eng. Radiat. Sci.* **2025**, *11*, 031401. [CrossRef]
11. Fu, Y.; Liu, Y.; Wang, J.; Wang, Y.; Xu, G.; Wen, J. Local resistance characteristics of elbows for supercritical pressure RP-3 flowing in serpentine micro-tubes. *Propuls. Power Res.* **2024**, *13*, 245–256. [CrossRef]
12. Liu, B.; Wu, Y.T.; Ma, C.F.; Meng, Y.; Hang, G. Turbulent convective heat transfer with molten salt in a circular pipe. *Int. Commun. Heat Mass Transf.* **2009**, *36*, 912–916. [CrossRef]
13. Srivastava, A.K.; Vaidya, A.M.; Maheshwari, N.K.; Vijayan, P. Heat transfer and pressure drop characteristics of molten fluoride salt in circular pipe. *Appl. Therm. Eng.* **2013**, *61*, 198–205. [CrossRef]
14. Ferng, Y.M.; Lin, K.Y.; Chi, C.W. CFD investigating thermal-hydraulic characteristics of FLiNaK salt as a heat exchange fluid. *Appl. Therm. Eng.* **2012**, *37*, 235–240. [CrossRef]
15. Li, S.J.; Zhou, C.Y.; Li, J.; Pan, X.-M.; He, X.-H. Effect of bend angle on plastic limit loads of pipe bends under different load conditions. *Int. J. Mech. Sci.* **2017**, *131–132*, 572–585. [CrossRef]
16. Wang, S.; Shi, R.; Wu, J.; Yang, C.; Liu, H. Investigation on optimization of finite element model for stress analysis of 12Cr1MoV main steam pipeline elbow. *Crystals* **2025**, *15*, 207. [CrossRef]
17. Kim, S.W.; Jeon, B.G.; Hahm, D.G.; Kim, M. Failure behavior for the thickness change of pipe elbows in nuclear power plant piping system. *Int. J. Press. Vessels Pip.* **2025**, *218*, 105626. [CrossRef]
18. Kim, S.H.; Choi, J.B.; Park, J.S.; Choi, Y.-H.; Lee, J.-H. A coupled CFD-FEM analysis on the safety injection piping subjected to thermal stratification. *Nucl. Eng. Technol.* **2013**, *45*, 237–248. [CrossRef]
19. Zhang, Y.; Lu, T. Unsteady-state thermal stress and thermal deformation analysis for a pressurizer surge line subjected to thermal stratification based on a coupled CFD-FEM method. *Ann. Nucl. Energy* **2017**, *108*, 253–267. [CrossRef]
20. Fuerst, T.; Bowers, A.; Gietl, H.; France, N.L.; Loftus, L.; Riet, A.A.; Eklund, M.D.; Taylor, C.N.; Shimada, M. The molten salt tritium transport experiment: A pumped fluoride salt loop for hydrogen isotope experimentation. *Ann. Nucl. Energy* **2025**, *223*, 111659. [CrossRef]
21. Becht, C.; Diehl, D.W. New piping flexibility rules in ASME B31.3, Appendix P. *J. Press. Vessel Technol.* **2006**, *128*, 84–88. [CrossRef]
22. Won, M.G.; Jeong, S.H.; Kim, K.; Huh, N.-S.; Lee, H.-Y.; Choi, J.-B. Development of creep elastic follow-up factor solutions for piping design of high-temperature reactor under combined primary and secondary loadings. *Int. J. Press. Vessels Pip.* **2020**, *182*, 104074. [CrossRef]
23. Abuhatira, A.A.; Salim, S.M.; Vorstius, J.B. CFD-FEA based model to predict leak-points in a 90-degree pipe elbow. *Eng. Comput.* **2023**, *39*, 3941–3954. [CrossRef]
24. Solomon, I.; Dundulis, G. Modeling of pipe whip phenomenon induced by fast transients based on fluid–structure interaction method using a coupled 1D/3D modeling approach. *Appl. Sci.* **2023**, *13*, 10653. [CrossRef]
25. Shih, T.H.; Liou, W.W.; Shabbir, A.; Yang, Z.; Zhu, J. A new k-ε eddy viscosity model for high Reynolds number turbulent flows. *Comput. Fluids* **1995**, *24*, 227–238. [CrossRef]

26. ASME. *ASME Boiler and Pressure Vessel Code, Section II: Materials, Part D: Properties (Metric)*, 2025 ed.; The American Society of Mechanical Engineers: New York, NY, USA, 2025.
27. Cutuli, P.; Cristaudo, A.; Bevilacqua, P.; Ferraro, V.; Settino, J.; Morrone, P. Energy analysis of novel hybrid solar, biomass, and natural gas combined cycle plants. *Energy* **2026**, *342*, 139597. [CrossRef]

Disclaimer/Publisher's Note: The statements, opinions and data contained in all publications are solely those of the individual author(s) and contributor(s) and not of MDPI and/or the editor(s). MDPI and/or the editor(s) disclaim responsibility for any injury to people or property resulting from any ideas, methods, instructions or products referred to in the content.